Materials & Design 238 (2024) 112630

Contents lists available at ScienceDirect

Materials & Design

journal homepage: www.elsevier.com/locate/matdes

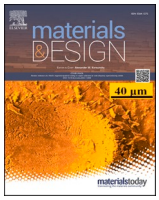

Understanding the damage initiation and growth mechanisms of two DP800 dual phase grades

Chunhua Tian [a,1,*], Carl F. Kusche [b,c], Angelica Medina [b], Subin Lee [b], Maximilian A. Wollenweber [c], Reinhard Pippan [d], Sandra Korte-Kerzel [c], Christoph Kirchlechner [a,b]

[a] Max-Planck-Institut für Eisenforschung GmbH, Max-Planck-Str. 1, 40237 Düsseldorf, Germany
[b] Institute for Applied Materials, Karlsruhe Institute of Technology, D-76344 Eggenstein-Leopoldshafen, Germany
[c] Institute for Physical Metallurgy and Materials Physics, RWTH Aachen University, 52062 Aachen, Germany
[d] Austrian Academy of Sciences, Erich Schmid Institute of Materials Science, Jahnstraße 12, Leoben 8700, Austria

ARTICLE INFO

Keywords:
Dual phase steel
Damage initiation
Void growth
Ferrite hardening

ABSTRACT

Dual phase (DP) steels are amongst the most widely used structural steels for automotive applications. It is essential to understand the damage initiation and damage growth in these high strength steels and further shed light on improving mechanical properties. In this work, two DP800 dual phase grades are investigated, which exhibit identical ultimate tensile stress but significantly different elongation in the uniaxial tensile test. To explain the difference in ductility, particularly described by uniform elongation, we investigate the damage initiation and growth mechanisms by analyzing microstructural changes upon deformation, such as voids, dislocation structures and the grain morphology. Furthermore, ferrite micropillars in pre-strained samples are tested *in situ* to capture the strain hardening capability of ferrite. We found that the DP steel with harder martensite and softer ferrite exhibits more damage initiation sites after deforming to an identical strain. However, void growth is much slower compared to the DP steel grade with fewer initiation sites. We explain the suppressed void growth by significant strain-hardening of ferrite surrounding the voids, which is observed in the micropillar compression experiments. The improved strain hardening of ferrite originates primarily from the difference in chromium content considering the negligible influence of dispersed particles.

1. Introduction

DP steels, comprised of soft ferrite and hard martensite, are widely applied in automotive manufacturing due to outstanding mechanical properties, such as high strength, continuous yielding and good formability, while equally showing strain-hardening potential [1,2]. However, similar to other structural materials, finding the optimal trade-off between strength and ductility is a challenging task. There are two effective approaches in DP steels to increase the strength, namely, decreasing the grain size and increasing the volume fraction of martensite [3–6], whereas there is on-going debate on how to improve ductility. For instance, the effects of grain size on the elongation of DP steels have not fully been understood. Calcagnotto et al. reported that grain refining of ferrite from 12 μm down to 1.2 μm hardly affects the uniform and total elongation [3,7], while Mondal et al. claimed that DP steels with coarse grains up to 60 μm show less ductility than those with 10 μm [5]. With respect to the effect of martensite phase volume, it is reported that an increase of the harder phase content up to 77 vol% results in a higher fracture strain [8] although with less uniform elongation. On the other hand, Pouranvari found the optimum martensite volume fraction that leads to the best ductility to be around 40 vol% [9]. These controversial debates suggest that it is still far from sufficient to inform on DP steels' ductility simply from grain size and martensite volume fraction, since one of the most important microstructural features which affects the ductility of alloys is the prevalence of microstructural damage, either as crack or void. It is important to understand their formation and growth mechanisms. Damage initiation and evolution depend on the local mechanical properties of the constituent. For

* Corresponding author.
E-mail address: chunhua.tian@empa.ch (C. Tian).
[1] Current address: Empa, Swiss Federal Laboratories for Materials Science and Technology, Laboratory for Mechanics of Materials and Nanostructures, Feuerwerkerstrasse 39, 3602, Thun, Switzerland.

https://doi.org/10.1016/j.matdes.2024.112630
Received 21 September 2023; Received in revised form 16 December 2023; Accepted 1 January 2024
Available online 3 January 2024

instance, using scanning electron microscopy (SEM), X-ray microtomography or digital imaging correlation, damage in DP steels initiates preferentially at stress concentrators such as hard martensite islands, ferrite/martensite phase boundaries or surroundings of hard inclusions [10–15]. As a commonality, the previous studies on this topic, however, tend to be non-quantitative [16,17], specifically lack of the local properties and further correlation with damage initiation and evolution.

In this work, we focus on quantitatively understanding damage initiation and evolution in two DP800 steels grades [18], with the same ultimate strength but different uniform elongation (larger elongation and better ductility desired). The samples are differently pre-strained so that we can have a statistical analysis of damage with straining. Furthermore, we performed microstructural characterization and micromechanical investigation on ferrite at different pre-strains to correlate the damage initiation/growth with the local mechanical properties. Note that the micromechanical investigation focuses on ferrite rather than martensite, which is based on two aspects: first, with similarity in grain size and martensite volume fraction, the main difference of two DP steels lies in the ferrite strength [18]. Second, as the strain hardening rate plays a dominant role in materials' ductility, the plastic deformation of the harder martensite islands is supposed to contribute much less than the soft ferrite [19–21]. For statistical analysis, large-area images are analyzed by machine learning based feature detection. For microstructure characterization, SEM, electron backscattered diffraction (EBSD), and electron channeling contrast imaging (ECCI) are applied. For micromechanical property, micropillar compression is performed on ferrite pillars extracted from pre-strained samples, which can capture the evolution of ferrite yield strength with increasing global strains.

2. Experimental procedures

2.1. Material of DP800 steels

Two DP800 steels (Ultimate Tensile Strength, UTS: 800 MPa) from different manufacturers are studied in this work. They are named as DP1 and DP2 in the following sections. By wet chemistry [18], DP1 has the nominal chemical composition of Fe-0.13C-1.51Mn-0.21Si-0.03Al (wt. %) while DP2 of Fe-0.13C-1.69Mn-0.19Si-0.03Al-0.7Cr-0.03Ti (wt. %). So chemically, DP2 has an extra addition of Cr and a small amount of Ti.

To investigate and understand the damage initiation and evolution in two DP steels, they are both pre-strained by an electromechanical testing machine (DZM in house built) and the strains were measured as the global strain over the deformed sample area based on the elongation between two markers in the undeformed parts of the samples. All pre-strained samples have a gauge length of 3.65 mm, a width of 1.5 mm and a thickness of 1.5 mm. For the pre-strain, the samples were continuously tested to the targeted point without interruption. It should be noted that the small dimension of pre-strained samples is applied based on the limited stage size for *in situ* deformation, from which a comparability of strains and damage between *in situ* and *ex situ* can be made in a previous publication [16]. Although in this work, *in situ* mesoscopic tension is not performed, we use the same dimensions for comparison. All the materials used in this study, the as-received (AR) state and pre-strained are listed in Table 1, corresponding to the applied investigation techniques.

2.2. Macroscopic uniaxial tensile tests

Macroscopic uniaxial tensile tests were performed on the as-received samples to compare the mechanical properties of two DP steels, in particular, the strain hardening rate. The tests follow the standard of DIN 50125-E with a gauge length of 26 mm, a sample width of 15 mm and a thickness of 1.5 mm. The reduction in area (%) of these two specimens presented here is approximately measured by a caliper.

Table 1
Overview of investigation methods performed at the global strain indicated in the table for both DP steel grades. Apart from the as-received samples (AR), all the rest are pre-strained to different macro strains. ML represents the abbreviation of machine learning, EBSD of electron backscattered diffraction and ECCI of electron channeling contrast imaging.

	Macro. tension	ML Damage size	EBSD	ECCI	Pillar compression
DP1	AR	17 %	AR, 18 %	AR, 5 %,10 %	AR, 19.4 %
DP2	AR	17 %	AR, 18 %	AR, 5 %,10 %	AR, 9.6 %, 14.6 %, 21.6 %

2.3. Microstructural characterization

For the microstructural investigation and the micromechanical tests, the center part of the two DP steels at different pre-strains were cut by wire erosion (approximately with a length of 3.6 mm, a width of 1.5 mm and a thickness 1.5 mm) and the side face along the tensile direction/rolling direction was ground and polished with oxide polishing suspension (OPS). An extra vibropolishing step was implemented with Mastermet 2 for EBSD and ECCI investigation.

Microstructures were analyzed using a field emission scanning electron microscope (Gemini500®) using the secondary electron (SE) and InLens® detectors. EBSD was performed on Zeiss Auriga® microscope equipped with an EDAX system with Hikari® charged coupled device (CCD) and the TSL OIM 7 software package. The parameters for EBSD were set as followed, acceleration voltage of 15 kV, aperture size 120 μm and step size 100 nm for the as-received samples while 20 kV, 60 μm and 40 nm for pillars and the pre-strained samples. The probe current was 1.1nA. The ECCI images were recorded using a Zeiss Merlin field emission microscope at 20 kV. The probe current was 3nA and working distance 6.1 mm. The fractographs were taken on a Tescan Mira scanning electron microscope.

The damage sites were detected, measured and analyzed via a deep-learning based framework first presented in [16]. The algorithm used is capable of discriminating between both deformation-induced damage and inclusions, as well as distinguishing the individual mechanisms of damage initiation, such as the fracture of martensite, and the decohesion of interface boundaries. In this work, it was applied to detect the voids, and set up void size statistics of the deformation-induced voids only.

2.4. Micromechanical pillar compression

Micromechanical tests were conducted on single crystalline ferrite pillars (2 μm in diameter) which were produced on two DP steels after a nominal pre-strain of 0 % and approximately 20 %. Ferrite is distinguished from martensite based on the contrast changing owing to the slight etching effect after ops polishing. Micropillars were fabricated using Ga^+ focused ion beam (FIB, Zeiss Auriga) and were localized in the center part of the polished surface. The aspect ratio of height and diameter was targeted to be between 2 and 2.5. A three-step milling strategy was applied, 16nA for coarse milling, 2nA for intermediate step and 600 pA for fine milling. Consecutively, EBSD was performed on the top of pillars to obtain crystallographic orientation information for the loading direction and the slip trace analysis after deformation. Additionally, for DP2, ferrite micropillars were also milled from the 9.6 % and 14.6 % pre-strained samples. The choice of 2 μm pillar diameter instead of larger sizes was due to the decreased grain size perpendicular to the macroscopic straining direction with increased pre-strains, still ensuring single crystalline micro pillars.

All *in situ* SEM micropillar compression tests were performed with an Asmec Unat II indenter (Asmec GmbH, Radeberg, Germany) which was installed in the Gemini 500. All experiments were carried out in a displacement-controlled mode with the strain rate of $1 \times 10^{-3} \bullet s^{-1}$, and a flat diamond tip (Synton MDP, Nidau, Switzerland) with a diameter of

5 μm was used. To obtain the engineering stress versus engineering strain curves, the load was divided by the area of the top surface and the displacement by the initial pillar height.

3. Results

3.1. Macroscopic uniaxial tensile test on as-received samples

The ultimate tensile strength is approximately 800 MPa for both DP steels in the as-received state (based on engineering stress-engineering strain, see Fig. 1), as given by the norm DP800. DP1 yields at higher stress compared to DP2, as magnified by the inset in Fig. 1 and remains stronger until reaching the necking instability point U1. The instability point is determined by the Considère criterion, as the intersection of strain hardening rate and true stress-true strain curve. A high initial strain hardening rate is observed for both DP steels and decreases rapidly with increasing strain. However, DP1 holds a smaller strain hardening rate than DP2 after experiencing a strain exceeding 1 %, resulting in an earlier necking instability (compare U1 9.8 % and U2 13.4 %, Fig. 1) and consequently a shorter uniform elongation. Noteworthy as well is that based on the engineering stress-engineering strain curves, DP2 can experience longer elongation to fracture (fracture elongation 19.1 % for DP1 and 23.1 % for DP2 based on two repeated tests). By measuring with a caliper, the two samples after tensile test fracture in Fig. 1 have a reduction in area of 37 % for DP1 and 39 % for DP2.

3.2. Statistics of damage initiation and growth in two DP steels

A machine-learning (ML) based approach is applied to statistically characterize emerging voids in the microstructure after deformation. This framework is capable of detecting and characterizing the voids in three steps, these being detected, differentiating between deformation-induced damage (by co-deformation of ferrite and martensite) and voids originating from inclusions, and finally discriminating between the various mechanisms of damage formation (details in [16]). The results of the classification of inclusion voids and deformation-induced damage has, for the DP1 microstructure, been checked by a human evaluator and corrected where necessary, in order to achieve a maximum classification accuracy on both microstructures. Fig. 2 shows the micrographs of two pre-strained DP steels after 17 %. After the same pre-strain, larger damage sites are visible in DP1 under the same magnification (B1 in Fig. 2a) and tend to connect with one another. Commonly for both samples, the main fundamental damage mechanisms are identified as the fracture of martensite islands (particularly

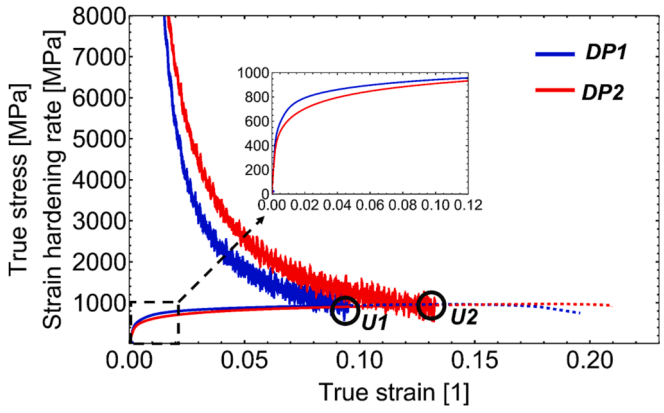

Fig. 1. True stress-true strain curves and strain hardening curves of two DP steels, with dashed segments after uniform deformation point. The strain hardening data is omitted after uniform deformation. The inset magnifies the initial segment of true stress-true strain curves.

those along the banding region as outlined by B1 and B2 in Fig. 2), or the decohesion of interfaces (martensite/ferrite phase boundary, matrix/inclusion interface), as representatively highlighted in Fig. 2c, d. Interestingly, the void size in DP1 seems to have a more continuous size spectrum (Fig. 2c1-3), while there tends to have a size jump in DP2, much smaller for voids induced by co-deformation of ferrite and martensite (Fig. 2d1) than by those clearly inclusion-related (Fig. 2d2, 3). These inclusion-related voids can be differentiated, as mentioned above, by the machine-leaning based framework, and will be excluded for the analysis of the subsequent size and area evolution.

The number of damage initiation sites per observed area is quantified with respect to the imposed strain (Fig. 3a). Here, we only take into account the deformation-induced sites. While the number of damage sites increases for both samples, DP2 has more damage sites over the whole strain range and features a much higher damage formation rate compared to DP1, especially starting from 10 % plastic strain [16]. However, in terms of the void size, the trend is the opposite (Fig. 3b, 17 % strained). This distinct difference in the evolution of the total number of induced voids calls for a thorough statistical investigation of both the origin and the sizes of the emerging voids in both steel grades, which yields the data presented in Fig. 3b. After 17 % strain, half of voids in DP2 are smaller than 2 μm^2 and the largest ones do not exceed 10 μm^2, consistent with a previous void size analysis on this material in [16]. However, in DP1, which has fewer damage initiation sites, the median value of deformation-induced void size reaches 15 μm^2 and the maximum observed void area even surpasses 60 μm^2. The whole cumulative curve of DP1 also exhibits a much wider distribution after experiencing an identical pre-strain. The statistical output by the machine-learning matches well with the information given in Fig. 2.

It should be noted that the much larger strain value over 30 % (fracture elongation 40 % for DP1 and 35 % for DP2), compared with the standardized tests, is induced by the significantly smaller sample size with different gauge section aspect ratio. Representative tensile curves for specimens in dimension of 3.6 x 1.5 x 1.5 mm^3 are provided as the supplementary figure (Fig. S1), demonstrating that at this size, both samples fractured at a strain over 30 %. However, the uniform elongation seems less influenced by the test geometry, comparing U1 ~ 14 % and U2 ~ 17 % (Fig. S1) obtained from the small samples with that (U1 ~ 10 %, U2 ~ 13 %) from large standard ones in Fig. 1.

3.3. Grain size & dislocation evolution

As statistically observed, the two DP steels exhibit a noticeably different damage initiation and evolution trend. Further microstructural investigation is performed to gain an insight into the possible contributing factors, particularly focused on the grain size and dislocation structure evolution upon straining, which are the critical features to track back the damage evolution history in two DP steels.

Fig. 4 shows the microstructure evolution taken by EBSD upon straining. As a reference, the microstructure (IQ map) in the as-received state is presented as well in Fig. 4a, d. In an IQ map, a lighter color represents ferrite while darker denotes martensite islands as marked by F and M, respectively, on Fig. 4a, d. The dark contrast occurs as the hard phase (martensite) contains a large number of dislocations and subboundaries which deteriorate the quality of a diffraction pattern (dark on IQ map) [22]. In the as-received state, ferrite of both steels exhibits an approximately equi-axed morphology (Fig. 4a, d), which evolves into more elongated grains along the tensile direction after 18 % pre-straining (Fig. 4b, e). Inside ferrite grains, we can also see subboundaries as indicated by arrows. Comparing the two DP steels, the most distinguishable difference is that ferrite in DP2 deforms in a more homogenous fashion and evolves into finer subgrains (Fig. 4c, f). As highlighted as R1 and R2, the two regions in DP1 show contrasted grain size, much coarser in R1, which indicates the inhomogeneous deformation of ferrite in DP1. Martensite islands in both samples, the dark features due to the low image quality, also rearrange themselves along

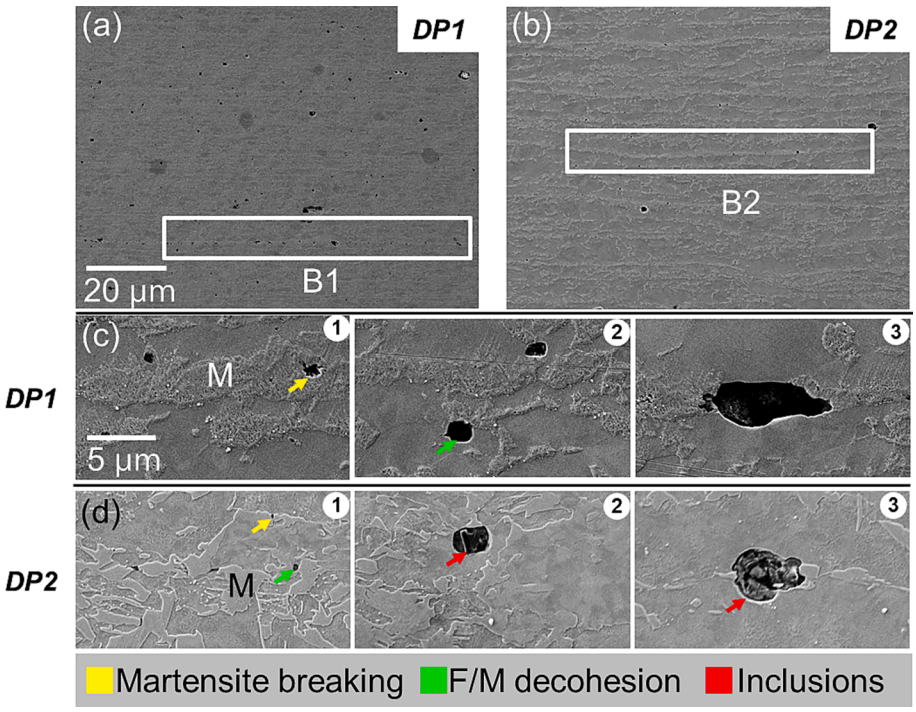

Fig. 2. (a, c) SEM micrograph showing voids in DP1 at 17% strain at two magnifications; (b, d) SEM micrographs showing voids in DP2 at 17% strain at two magnifications. B1 and B2 outline voids along banded martensite in DP1 and DP2, respectively.

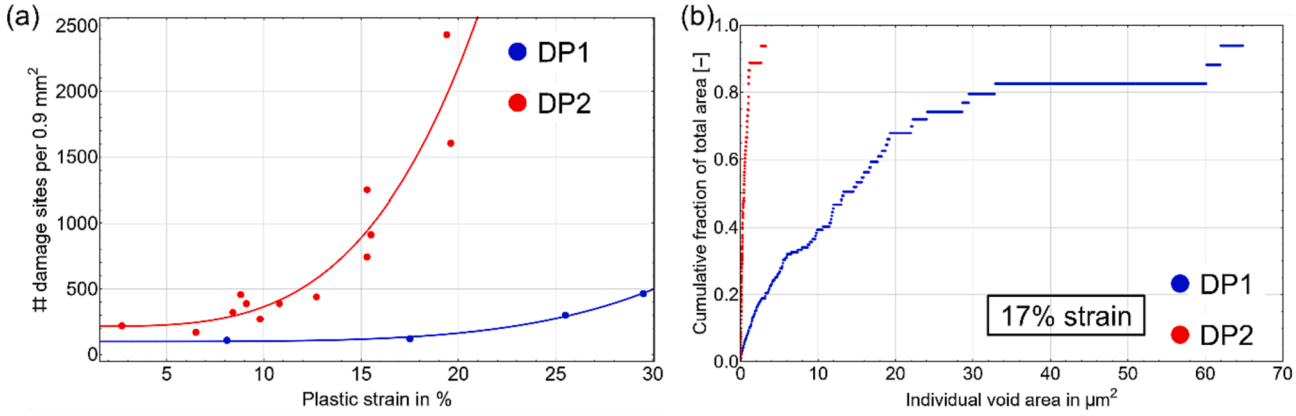

Fig. 3. (a) Number of deformation-induced voids over strain in DP1 and DP2 (reproduced from [16]); (b) Cumulative void size probability normed to individual void size in both DP steel grades after a 17% straining.

the pre-straining direction (Fig. 4b, e).

ECCI is applied further on both pre-strained DP steels to have a closer look on the dislocation evolution inside ferrite grains with straining. After 5 % deformation, while ferrite grains in the two DP steels still show predominant, densely tangled dislocations (Fig. 5 a, c), there is a more significant sign of dislocation wall structures in DP1 (arrow in Fig. 5a). However, at this point, inside the wall-outlined region, a large number of disordered dislocations still exists. Upon further deformation to 10 %, the dislocation wall in DP1 seems well-developed into cell structures. Inside these cells, the dislocation density is largely reduced (Fig. 5b). After 10 % pre-straining of DP2, to a lesser extent, dislocation cells also start to develop, as we can still see a magnitude of dislocations inside the cells. For instance, comparing R1 in Fig. 5b and R2 in Fig. 5d, there are much more bright lines and dots in R2 (DP2), representing a higher dislocation density. Apart from the dislocation evolution, small particles are also spotted in both DPs, which tend to locate in areas with high dislocation density (arrows in Fig. 5b, d).

Particles can influence the movement of dislocations and resulting mechanical properties. Therefore, these particles are statistically analyzed from ECCI images to have a quantitative understanding of their contribution to the observed mechanical difference between the two DP steels. Only those smaller than the micrometer sized inclusions are considered. Due to the big differences in the particle number and size between DP1 and DP2, the particle analysis used different magnifications and as a result, different total investigation areas. For DP1, five ECCI images with each observation area 57.5 x 43.1 μm^2 were analyzed while for DP2, eight ECCI images with each 5.75 x 4.31 μm^2 were investigated. Fig. 6 shows the distribution of the particles in two DP steels. We found that DP2 contains much finer particles and the particle size shows a more constrained distribution; the particle size in DP2 is 49.9 ± 28.1 nm (mean plus standard deviation) with a spacing of 2.3 ± 0.4 µm while in DP1 the size is 136.2 ± 71.7 nm with an average spacing of 12.4 ± 1.4 µm. The particle contribution to hardening was estimated based on Orowan strengthening (bowing stress), resulting in an Orowan

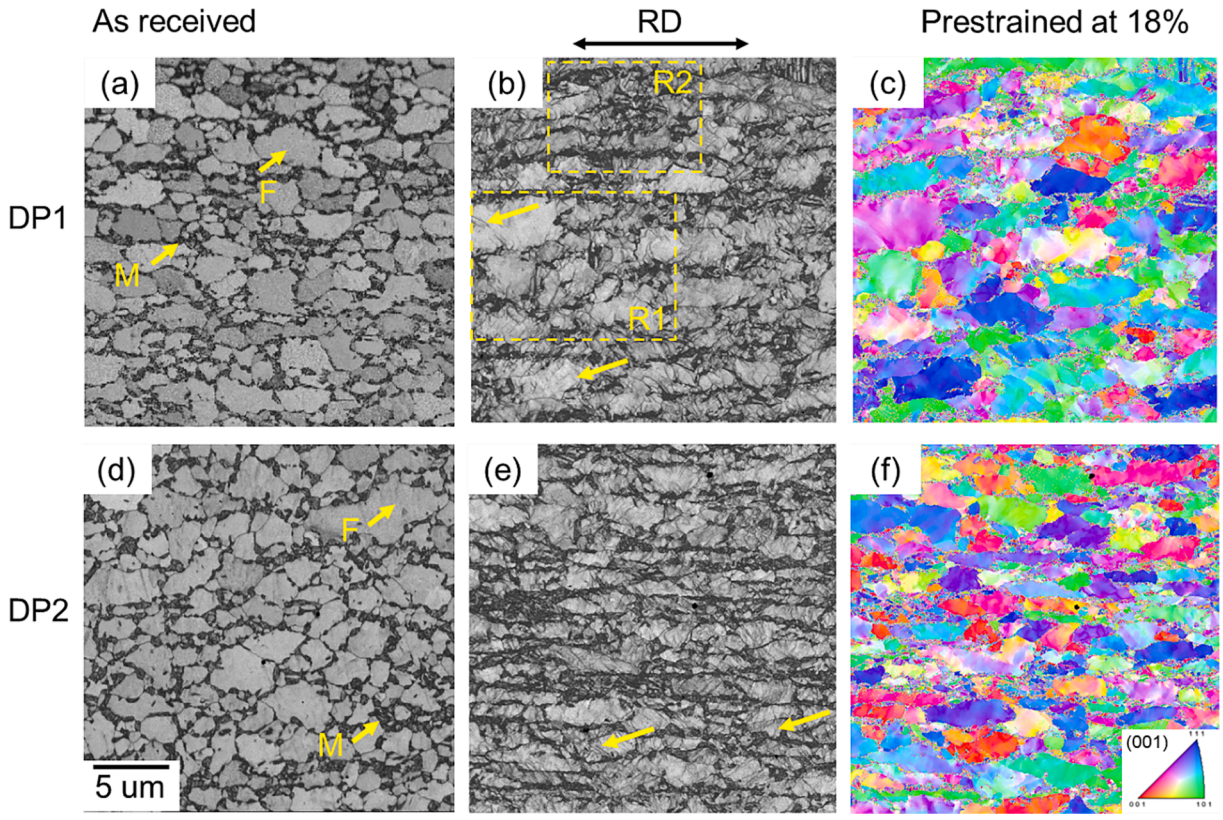

Fig. 4. (a) Image quality (IQ) map of DP1 in as-received state; (b) IQ and (c) inverse pole figure (IPF) maps of DP1 pre-strained at 18%; (d) IQ map of DP2 in as-received state; (e) IQ and (f) IPF maps of DP2 pre-strained at 18%. Arrows in (a, d) differentiate ferrite and martensite phase while in (b, e) exemplarily indicate the subboundaries formed during straining. The rolling direction is horizontal and the tensile direction is along the rolling direction.

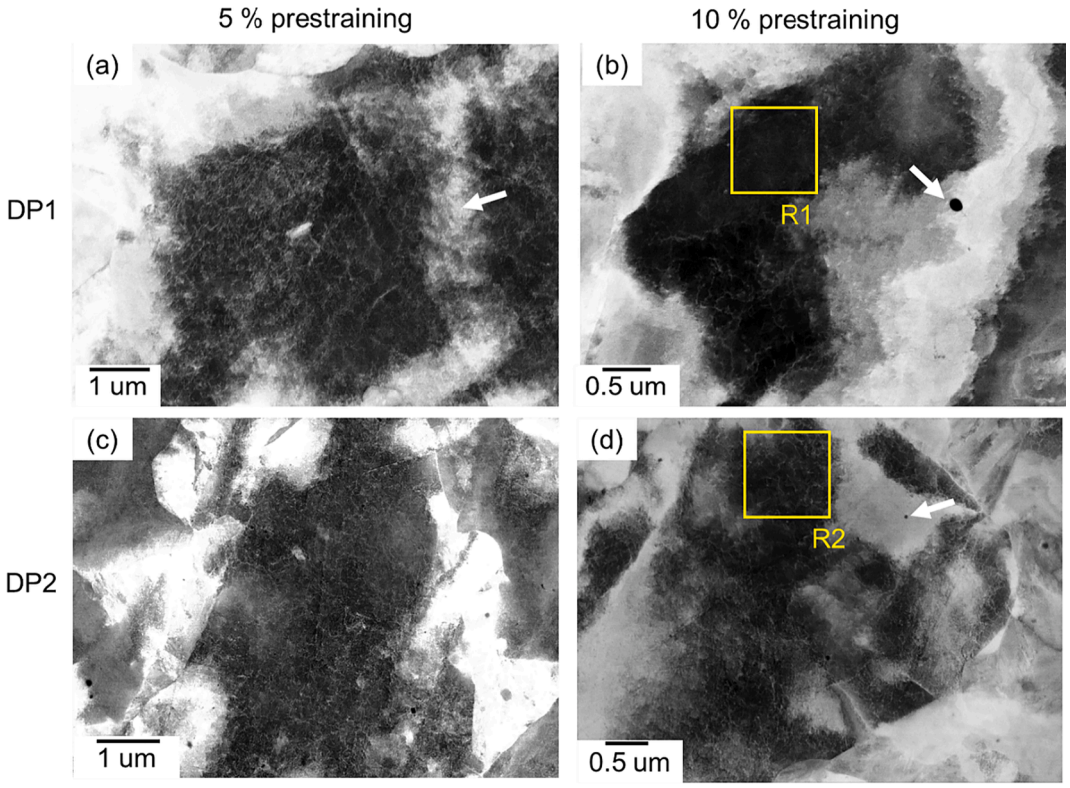

Fig. 5. Dislocation structures in ferrite grains resolved by ECCI for (a) 5 %; (b) 10% pre-strained in DP1 and (c) 5%; (d) 10% in DP2. The arrows in (a) refer to a dislocation wall while in (b) and (d) indicate dispersed particles.

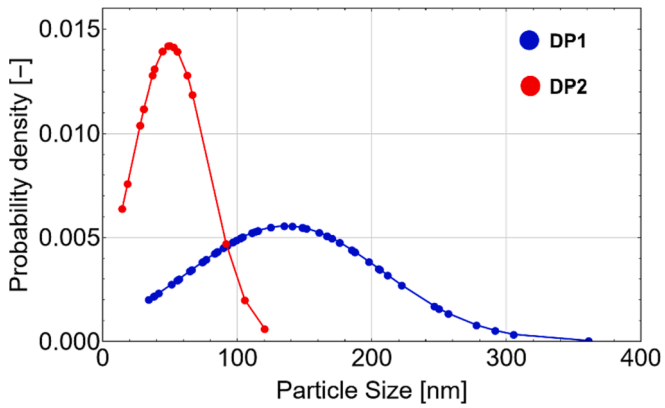

Fig. 6. Distribution of particle size for DP1 and DP2.

stress of 0.9 MPa for DP1 and 5 MPa for DP2 [23]. Therefore, we conclude that the contribution of these particles on strengthening is negligible in both DP steels.

3.4. Micromechanical pillar compression on pre-strained samples

Combined with the statistics of damage sites and further microstructural characterization, while DP2 has more damage sites but they grow at a slower rate with pre-straining, ferrite in this steel tends to demonstrate a slower rearrangement of dislocations into more ordered cell structures and further into subgrains. This indicates ferrite in DP2 is likely to exhibit a higher strain hardening potential, which motivates us to have a quantitative investigation by site-specific micromechanical tests.

For that, pillar compression tests were performed on ferrite of different pre-strained DP steel samples. Note that the pre-straining is necessary to investigate the strain hardening capability of ferrite, as pillar compression is well-suited to extract the yield strength of small volumes but not appropriate to directly capture the true strain hardening behavior. The extracted work hardening values from pillar compression are affected by constrains from the setup and therefore termed "apparent strain hardening" [24].

Fig. 7 shows representative micro pillars tested and their stress–strain curves for DP1 and DP2 after 19.4 % and 21.6 % pre-strain, respectively. To track the ferrite hardening with pre-straining of the two DP steels, micropillars from single ferrite grains were extracted, as shown in Fig. 7a, d. The loading direction of the two pillars is ⟨835⟩ and ⟨619⟩, respectively. Combined with the *in situ* recording and slip steps on pillars, the identified primary slip system in Fig. 7b, e is $(110)[\bar{1}11]$ and $(132)[1\bar{1}1]$, with the respective Schmid factor 0.47 and 0.50. The yield stress extracted at 2 % plastic strain is 730 MPa for the pillar in Fig. 7a and 860 MPa for pillar in Fig. 7d (Fig. 7c, f). From the Schmid factor of the activated slip systems, the calculated critical resolved shear stress (CRSS) for these two pillars is 340 MPa and 430 MPa.

The cumulative distribution of CRSS is calculated from 49 DP1 ferrite pillars (20 at 0 %; 29 at 19.4 % pre-strain) and 44 DP2 ferrite pillars (22 at 0 %; 22 at 21.6 % pre-strain) to statisticaly analyze the changes of CRSS upon pre-straining, (Fig. 8). Compared with the as-received state, pre-straining hardens ferrite significantly for both DP steel grades. While the CRSS of ferrite in DP1 increases from 266 ± 15 MPa to 336 ± 14 MPa upon 19.4 % pre-straining, in DP2 it rises from 226 ± 9 MPa to 386 ± 11 MPa after 21.6 % pre-strain. Hence, at a comparable pre-deformation, ferrite in DP2 demonstrates a much higher work hardening with approximately 26 % increase in CRSS for DP1 while up to 70 % for DP2. Noteworthy also is that the CRSS distribution width of ferrite in DP1 is significantly broader than in DP2 after pre-straining, specifically, 85.7 ± 2.9 MPa distribution width at 19.4 % pre-strain of DP1 and 55.3 ± 2.4 MPa at 21.6 % pre-strain of DP2. The broadened distribution of CRSS in DP1, in fact, correlates well with the EBSD results in Fig. 4, where the ferrite in DP1 deforms in an inhomogeneous way.

Ferrite pillars from 9.6 % (15 pillars) and 14.6 % (18 pillars) pre-strained DP2 were also successfully tested. Fig. 9a shows CRSS distribution in DP2 at four states, as-received, pre-strained at 9.6 %, 14.6 % and 21.6 %. With an increased imposed pre-strain, the strength of ferrite is also increased. Further, in all cases, they have a comparable distribution width indicating homogeneous deformation of ferrite even at different pre-straining stages. As a summary, the mean value of CRSS and the standard deviation corresponding to each tested sample state are listed in Table 2. Fig. 9b plots the CRSS of ferrite against an average

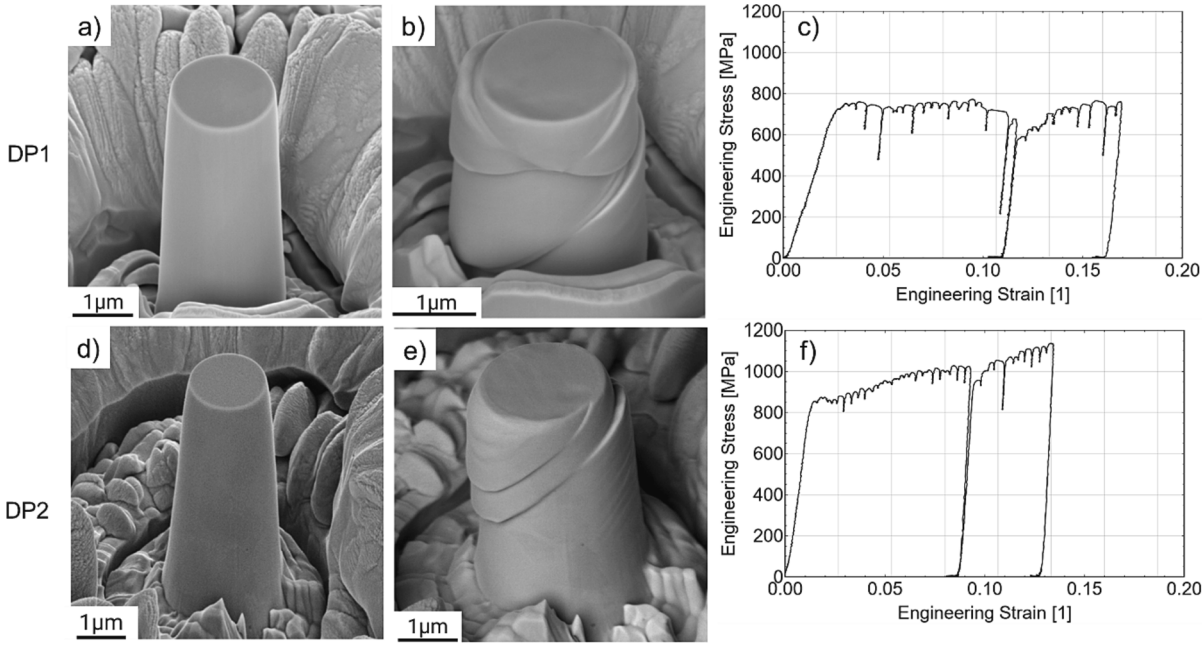

Fig. 7. Representative micropillars in the as-milled state (a, d) and post-mortem from the pre-strained sample (b, e), together with the corresponding engineering stress-engineering strain curve (c, f). The first row (a-c) refers to 19.4% pre-strained DP1 while the second row (d-f) represents 21.6% pre-strained DP2.

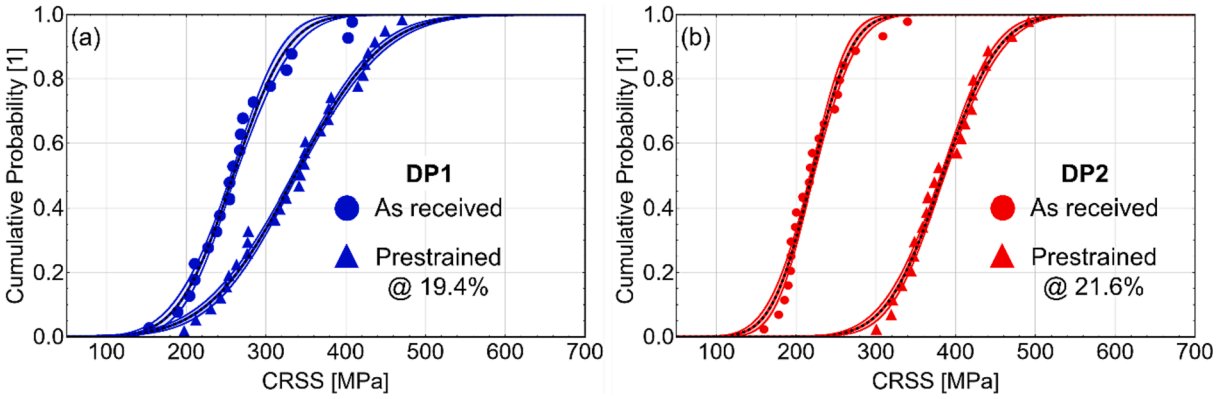

Fig. 8. Cumulative distribution of CRSS for (a) ferrite of DP1 in as-received state and after 19.4% pre-straining; (b) ferrite of DP2 in as-received state and after 21.6% pre-straining.

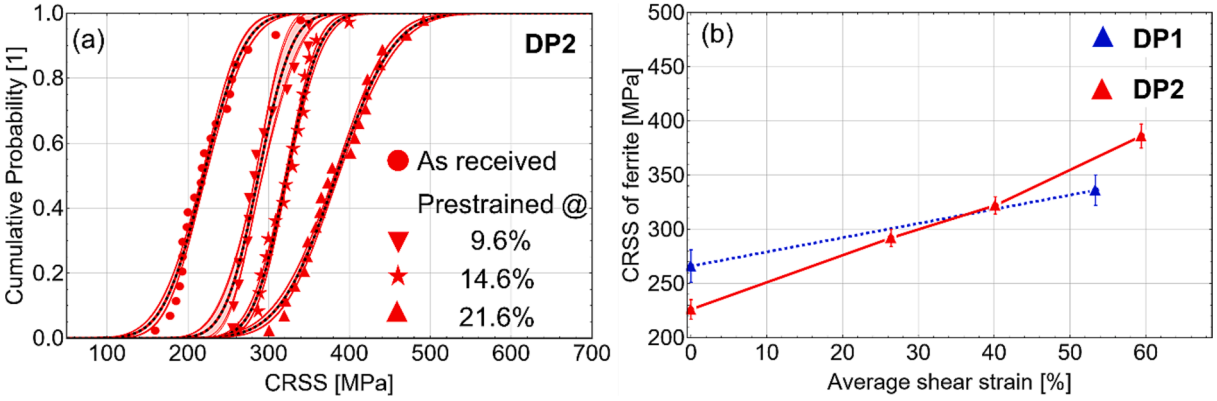

Fig. 9. (a) Cumulative distribution of CRSS for ferrite in DP2 upon different pre-straining. (b) The yield strength of ferrite plotted against the average shear strain converted from the global pre-strain.

Table 2
CRSS of ferrite at different pre-strained states, as obtained from micropillar compression. The mean value and the standard deviation are given. In both cases the error bars are given as the standard error of the mean.

	Sample state	Mean value [MPa]	standard deviation [MPa]
DP1	As-received	266 ± 15	53.9 ± 3.1
	19.4 %	336 ± 14	85.7 ± 2.9
DP2	As-received	226 ± 9	39.4 ± 2.3
	9.6 %	292 ± 8	32.4 ± 3.7
	14.6 %	323 ± 8	32.3 ± 1.7
	21.6 %	386 ± 11	55.3 ± 2.4

shear strain for both DP steels. The average shear strain is approximated through multiplying the global pre-strain by a Taylor factor 2.75 based on the pencil glide slip of bcc structures ($\overline{\Gamma} = \overline{M}\bar{\varepsilon}$) [25,26]. Here,$\overline{\Gamma}$ represents the average shear strain in a single ferrite crystal embedded in randomly oriented ferrite polycrystals, which undergoes an average macroscopic strain of $\bar{\varepsilon}$ (taken as global strain here), and $\overline{M}$ is the average Taylor factor. Although there are not as many strain points tested in DP1 (plotted as dashed), it can serve as a more direct visualization on the strain hardening capacity of two steel grades. From the investigated strain targets, the hardening of ferrite in DP2 tends to have a linear behavior (see red connected points in Fig. 9b). Assume both DP steels have a similarly linear tendency, the slope of 265 MPa for DP2 is apparently higher than 131 MPa for DP1.

4. Discussion

The discussion focuses on understanding different damage initiation and damage growth phenomena in two DP steels and then a correlation with the observed macroscopic mechanical property, in particular, ductility described by uniform elongation, which is less dependent on tested sample size [27], as mentioned in the results section.

4.1. Damage initiation

In both DP steels, damage nucleates either at ferrite/martensite boundaries or inside martensite islands, in particular those along the martensite banding (Fig. 2). With a hard martensite and a soft ferrite matrix, DP steels can be regarded as a composite material. Previous work found that a lower yield strength of the matrix can promote the decohesion of phase boundaries [28,29]. The matrix with lower yield strength can plastically deform earlier and cause strain localization. In the case of DP steels, strain localization occurs most frequently at the phase boundaries and later correlates with damage initiation spots [30]. This matches well with our observation. On one hand, DP2 with a softer ferrite (higher mechanical heterogeneity) experiences a more homogeneous plastic deformation (Fig. 4e) and nucleates a higher number of damage sites after exposing to an identical global pre-strain (Fig. 3a). On the other hand, a part of ferrite grains in DP1 remains almost undeformed (Fig. 4b), providing fewer strain localization spots and consequently fewer damage nucleation sites. The more homogenous deformation of ferrite grains in DP2 probably results from a more uniform distribution of carbon due to the addition of Cr [31].

Apart from ferrite strength, the colony size of martensite islands

might also play a role in the damage initiation of two DP steels. With a comparable volume fraction, the slightly smaller colony size of martensite islands in DP2 (compare 1.1 ± 0.1 μm in DP2 to 1.0 ± 0.1 μm in DP1 [18]) indicates more phase boundaries, in other words, more weak points for damage nucleation. Similarly reported, the DP steel with smaller and scattered martensite initiates more damage compared to the counterpart displaying a more bulky morphology of the hard phase [30].

4.2. Damage growth

According to the fractography (Fig. S2), the two DP steels failed primarily in a ductile way, characterized by deep dimples. The ductile growth of damages is physically induced by the motion of dislocations to the newly created free surface [32]. Dislocation based plasticity and therefore the growth of ductile damage (see for instance [33]) is suppressed by alloying elements. The micro pillar experiments (see Figs. 8 and 9) are intended to shine light on the differences in strain hardening of ferrite in two DP steel grades. According to the pillar compression results, the strain hardening rate of ferrite single crystal pillars is roughly 265 ± 16 MPa in DP2 and 131 ± 17 MPa in DP1 (Fig. 9b), which demonstrates that ferrite in DP2 shows significantly more strain hardening after exposing to an identical pre-strain than DP1. Since the only notable difference of ferrite in DP1 and DP2 is the Cr content, it is concluded that Cr is the key contributor for strain hardening and, therefore, for the suppressed damage growth in DP2.

The strengthening effect of chromium in iron is also experimentally verified in literature. As reported by Riebisch et al. [34], the yield strength of iron increases noticeably by adding 0.6 wt% Cr (0.8 wt% Cr in DP2). Caillard *et al.* further directly observed in Cr iron (14 at.%) the dragging phenomenon of Cr on screw dislocations through *in situ* TEM straining [35]. The retarding effect of Cr on the dislocation motion delays the rearrangement of unlocked forest dislocations into more ordered substructures that are less effective for strain hardening (Fig. 5), similar with the case in [36], where dislocation cell structures are found by TEM to appear at a later stage in the fine Ti carbides containing DP steel. We do observe particles as well in the ferrite of two DP steels and there are differences in the number and size, but the distance between particles is not sufficiently short and the particles are not fine enough to induce a significant hardening effect and result in a different work hardening behavior (Fig. 6).

The beneficial effect of ferrite hardening on delaying damage growth is valid regardless of damage initiation sites. For damage initiated in martensite islands via martensite cracking, damage forms and propagates in a brittle manner along the martensite subboundaries, particularly, in the DP1 steel grade, decorated by Fe3C carbide [18]. After reaching the ferrite-martensite boundary or growing into ferrite, the ferrite work hardening will play a decisive positive role again in slowing down the damage growth. In fact, three-dimensional damage analysis suggests that most damage sites originate as martensite cracks and then grow into the ferrite phase [15].

4.3. Mechanical properties of DP steels

More damage initiation sites do not necessarily lead to an earlier necking (worse ductility), as evidenced in the case of DP2. The damage evolution process matters significantly, which is further related to the strain hardening capability of ferrite phase, specifically, the higher strain hardening rate of ferrite correlates with slower damage growth and better enhanced ductility. The assessment of ductility based on damage growth and ferrite strain hardening, in fact, aligns well with that evaluated according to the Considère criterion (macroscopic), which states that better ductility is achieved with higher overall strain hardening rate assuming a constant UTS. This coincidence implies that the strain hardening of DP steels is primarily dominated by ferrite deformation. By an approximate conversion of the tensile pre-strain to the average shear strain based on the Taylor model, the strain hardening rate of ferrite single crystal pillars is roughly 265 ± 16 MPa in DP2 and 131 ± 17 MPa in DP1 (Fig. 1), which gives (multiplied by M^2,$M = 2.75$) a strain hardening rate of 2 GPa and 1 GPa in the corresponding polycrystalline ferrite [37].

Apparently, the strain hardening rate during a micro compression test on a single crystal ferrite pillar is significantly smaller than the strain hardening rate of the DP steel (Fig. 1). The main reason is the unconstrained slip in single crystalline ferrite pillars due to free surfaces. Consequently, dislocations do not pile-up at interfaces (ferrite/martensite boundaries and grain boundaries), resulting in smaller CRSS due to a lack of back stress.

5. Conclusions

In this work, we aim at understanding damage initiation and damage growth mechanisms of two DP800 steels by investigating differently pre-strained samples. The investigation includes a statistical analysis of voids, microstructural characterization by EBSD and ECCI, and mechanical characterization of ferrite with pillar micro compression. Based on the experimental results, the following conclusions can be made:

1) Upon an identical global pre-strain, DP2 initiates significantly more damage sites due to a higher mechanical heterogeneity between ferrite and martensite.
2) The initiated damage sites in DP2 do not grow as fast as in DP1 owing to a larger strain hardening capacity of ferrite in the former.
3) The superior strain hardening in ferrite of DP2 primarily originates from the solid solution strengthening by the alloying element Cr. The effect of additional dispersed particles on strain hardening is negligible. This is evidently supported by a delayed emergence of ordered dislocation substructures in DP2.
4) Ductility of DP steels can be improved by suppressing void growth, which itself can be reached by enhancing the strain hardening of ferrite.

CRediT authorship contribution statement

Chunhua Tian: Writing – original draft, Software, Methodology, Investigation, Data curation, Conceptualization. **Carl F. Kusche:** Writing – original draft, Methodology, Investigation, Data curation, Conceptualization. **Angelica Medina:** Writing – review & editing, Methodology, Investigation, Data curation. **Subin Lee:** Writing – review & editing, Methodology, Investigation, Data curation. **Maximilian A. Wollenweber:** Writing – review & editing, Data curation. **Reinhard Pippan:** Writing – review & editing. **Sandra Korte-Kerzel:** Writing – review & editing. **Christoph Kirchlechner:** Writing – review & editing, Supervision, Project administration, Funding acquisition, Conceptualization.

Declaration of competing interest

The authors declare that they have no known competing financial interests or personal relationships that could have appeared to influence the work reported in this paper.

Data availability

Data will be made available on request.

Acknowledgements

This work is funded by the German research foundation (Deutsche Forschungsgemeinschaft, DFG) within the Collaborative Research Center (TRR 188, “Damage Controlled Forming Processes”, 278868966). Philipp Lennemann from Technische Universität Dortmund is acknowledged for the macroscopic tensile tests. Chunhua Tian is

grateful to Prof. Dr Johann Michler and Dr. Jakob Schwiedrzik for the equipment support at EMPA.

Appendix A. Supplementary data

Supplementary data to this article can be found online at https://doi.org/10.1016/j.matdes.2024.112630.

References

[1] C.C. Tasan, M. Diehl, D. Yan, M. Bechtold, F. Roters, L. Schemmann, C. Zheng, N. Peranio, D. Ponge, M. Koyama, An overview of dual-phase steels: advances in microstructure-oriented processing and micromechanically guided design, Annu. Rev. Mat. Res. 45 (2015) 391–431.
[2] N. Fonstein, Dual-phase steels, Automotive steels, Elsevier, 2017, pp. 169–216.
[3] M. Calcagnotto, Y. Adachi, D. Ponge, D. Raabe, Deformation and fracture mechanisms in fine-and ultrafine-grained ferrite/martensite dual-phase steels and the effect of aging, Acta Mater. 59 (2) (2011) 658–670.
[4] H. Li, S. Gao, Y. Tian, D. Terada, A. Shibata, N. Tsuji, Influence of tempering on mechanical properties of ferrite and martensite dual phase steel, Mater. Today:. Proc. 2 (2015) S667–S671.
[5] D. Mondal, R. Dey, Effect of grain size on the microstructure and mechanical properties of a C–Mn–V dual-phase steel, Mater. Sci. Eng. A 149 (2) (1992) 173–181.
[6] C. Peng-Heng, A. Preban, The effect of ferrite grain size and martensite volume fraction on the tensile properties of dual phase steel, Acta Metall. 33 (5) (1985) 897–903.
[7] M. Calcagnotto, D. Ponge, E. Demir, D. Raabe, Orientation gradients and geometrically necessary dislocations in ultrafine grained dual-phase steels studied by 2D and 3D EBSD, Mater. Sci. Eng. A 527 (10–11) (2010) 2738–2746.
[8] M. Mazinani, W. Poole, Effect of martensite plasticity on the deformation behavior of a low-carbon dual-phase steel, Metall. Mater. Trans. A 38 (2) (2007) 328–339.
[9] M. Pouranvari, Tensile strength and ductility of ferrite-martensite dual phase steels, Assoc. Metall. Eng. Serbia 16 (3) (2010) 187–194.
[10] A. Ramazani, A. Schwedt, A. Aretz, U. Prahl, W. Bleck, Characterization and modelling of failure initiation in DP steel, Comput. Mater. Sci. 75 (2013) 35–44.
[11] K. Alharbi, H. Ghadbeigi, P. Efthymiadis, M. Zanganeh, S. Celotto, R. Dashwood, C. Pinna, Damage in dual phase steel DP1000 investigated using digital image correlation and microstructure simulation, Model. Simul. Mater. Sci. Eng. 23 (8) (2015) 085005.
[12] E. Maire, O. Bouaziz, M. Di Michiel, C. Verdu, Initiation and growth of damage in a dual-phase steel observed by X-ray microtomography, Acta Mater. 56 (18) (2008) 4954–4964.
[13] J. Kang, Y. Ososkov, J.D. Embury, D.S. Wilkinson, Digital image correlation studies for microscopic strain distribution and damage in dual phase steels, Scr. Mater. 56 (11) (2007) 999–1002.
[14] H. Ghadbeigi, C. Pinna, S. Celotto, J. Yates, Local plastic strain evolution in a high strength dual-phase steel, Mater. Sci. Eng. A 527 (18–19) (2010) 5026–5032.
[15] S. Medghalchi, E. Karimi, S.-H. Lee, B. Berkels, U. Kerzel, S. Korte-Kerzel, Three-dimensional characterisation of deformation-induced damage in dual phase steel using deep learning, Mater. Des. 112108 (2023).
[16] C. Kusche, T. Reclik, M. Freund, T. Al-Samman, U. Kerzel, S. Korte-Kerzel, Large-area, high-resolution characterisation and classification of damage mechanisms in dual-phase steel using deep learning, PLoS One 14 (5) (2019) e0216493.
[17] C.F. Kusche, F. Pütz, S. Münstermann, T. Al-Samman, S. Korte-Kerzel, On the effect of strain and triaxiality on void evolution in a heterogeneous microstructure–A statistical and single void study of damage in DP800 steel, Mater. Sci. Eng. A 799 (2021) 140332.
[18] C. Tian, D. Ponge, L. Christiansen, C. Kirchlechner, On the mechanical heterogeneity in dual phase steel grades: activation of slip systems and deformation of martensite in DP800, Acta Mater. 183 (2020) 274–284.
[19] M. Kapp, T. Hebesberger, O. Kolednik, A micro-level strain analysis of a high-strength dual-phase steel, Int. J. Mater. Res. 102 (6) (2011) 687–691.
[20] S. Li, C. Guo, L. Hao, Y. Kang, Y. An, In-situ EBSD study of deformation behaviour of 600 MPa grade dual phase steel during uniaxial tensile tests, Mater. Sci. Eng. A 759 (2019) 624–632.
[21] C. Tian, C. Kirchlechner, The fracture toughness of martensite islands in dual-phase DP800 steel, J. Mater. Res. 36 (12) (2021) 2495–2504.
[22] S.I. Wright, M.M. Nowell, EBSD image quality mapping, Microsc. Microanal. 12 (1) (2006) 72–84.
[23] G. Gottstein, Physical foundations of materials science, Springer, 2004.
[24] G. Dehm, B.N. Jaya, R. Raghavan, C. Kirchlechner, Overview on micro-and nanomechanical testing: New insights in interface plasticity and fracture at small length scales, Acta Mater. 142 (2018) 248–282.
[25] J. Rosenberg, H. Piehler, Calculation of the Taylor factor and lattice rotations for bcc metals deforming by pencil glide, Metall. Trans. 2 (1) (1971) 257–259.
[26] U. Kocks, The relation between polycrystal deformation and single-crystal deformation, Metall. Mater. Trans. B 1 (1970) 1121–1143.
[27] Y. Zhu, X. Wu, Ductility and plasticity of nanostructured metals: differences and issues, Mater. Today Nano 2 (2018) 15–20.
[28] L. Babout, Y. Brechet, E. Maire, R. Fougeres, On the competition between particle fracture and particle decohesion in metal matrix composites, Acta Mater. 52 (15) (2004) 4517–4525.
[29] Y. Charles, R. Estevez, Y. Bréchet, E. Maire, Modelling the competition between interface debonding and particle fracture using a plastic strain dependent cohesive zone, Eng. Fract. Mech. 77 (4) (2010) 705–718.
[30] C.C. Tasan, J.P. Hoefnagels, M. Diehl, D. Yan, F. Roters, D. Raabe, Strain localization and damage in dual phase steels investigated by coupled in-situ deformation experiments and crystal plasticity simulations, Int. J. Plast. 63 (2014) 198–210.
[31] J.F.d. Silva Filho, C.A.S.d. Oliveira, N. Fonstein, O. Girina, F.J.F. Miranda, J. Drumond, E.A. Serafim, C.R.M. Afonso, Effect of Cr additions on ferrite recrystallization and austenite formation in dual-phase steels heat treated in the intercritical temperature range, Mater. Res. 19 (2016) 258–266.
[32] V. Lubarda, M. Schneider, D. Kalantar, B. Remington, M. Meyers, Void growth by dislocation emission, Acta Mater. 52 (6) (2004) 1397–1408.
[33] Y. Cui, Y. Toku, Y. Kimura, Y. Ju, High-strain-rate void growth in high entropy alloys: Suppressed dislocation emission= suppressed void growth, Scr. Mater. 185 (2020) 12–18.
[34] M. Riebisch, B. Pustal, A. Bührig-Polaczek, Impact of carbide-promoting elements on the mechanical properties of solid-solution-strengthened ductile iron, Int. J. Met. 14 (2020) 365–374.
[35] D. Caillard, A TEM in situ study of alloying effects in iron. II—Solid solution hardening caused by high concentrations of Si and Cr, Acta Mater. 61 (8) (2013) 2808–2827.
[36] S.-P. Tsai, C.-H. Jen, H.-W. Yen, C.-Y. Chen, M.-C. Tsai, C.-Y. Huang, Y.-T. Wang, J.-R. Yang, Effects of interphase TiC precipitates on tensile properties and dislocation structures in a dual phase steel, Mater. Charact. 123 (2017) 153–158.
[37] H. Mecking, U. Kocks, C. Hartig, Taylor factors in materials with many deformation modes, Scr. Mater. 35 (4) (1996) 465–471.